EEG-based Motor Imagery Decoding via Graph Signal Processing on Learned Graphs

Maliheh Miri, Vahid Abootalebi*, Hamid Saeedi-Sourck, Hamid Behjat

***Abstract*— *Objective:* This paper presents a graph signal processing (GSP)-based approach for decoding two-class motor imagery EEG data via deriving task-specific discriminative features. *Methods:* First, a graph learning (GL) method is used to learn subject-specific graphs from EEG signals. Second, by diagonalizing the normalized Laplacian matrix of each subject's graph, an orthonormal basis is obtained using which the graph Fourier transform (GFT) of the EEG signals is computed. Third, the GFT coefficients are mapped into a discriminative subspace for differentiating two class data using a projection matrix obtained by the Fukunaga-Koontz transform (FKT). Finally, an SVM classifier is trained and tested on the variance of the resulting features to differentiate motor imagery classes. *Results:* The proposed method is evaluated on Dataset IVa of the BCI Competition III and its performance is compared to i) using features extracted on a graph constructed by Pearson correlation coefficients and ii) three state-of-the-art alternative methods. *Conclusion:* Experimental results indicate the superiority of the proposed method over alternative methods, reflecting the added benefit of integrating elements from GL, GSP and FKT. *Significance:* The proposed method and results underpin the importance of integrating spatial and temporal characteristics of EEG signals in extracting features that can more powerfully differentiate motor imagery classes.**

***Index Terms*—— EEG, Fukunaga-Koontz Transform (FKT), Graph Learning, Graph Signal Processing, Motor Imagery.**

I. Introduction

ELECTROENCEPHALOGRAPHY (EEG) is a prevalent, non-invasive imaging modality for capturing brain activity at high temporal resolution [1]. A popular topic in analyzing EEG is during motor imagery (MI) tasks, which are dynamic states of movement imagination during which primary sensorimotor areas exhibit patterns of neural activity that resembles an attenuated version of real executed movement [2, 3]. From neurophysiological perspective, desynchronization of the neural populations during motor imagery tasks attenuates rhythms in the respective cortex and can be measured as a sign of brain activity [3, 4]. MI tasks are extensively utilized in brain-computer interface (BCI) systems, in which mental imagination of a movement is translated to executive commands via classification of features extracted from acquired EEG data [5-7].

Discrimination of mental states from EEG measurements in MI-BCI systems is a challenging task, for which numerous methods have been proposed [8]. One class of proposed methods aims at extracting features from the temporal evolution of the signal acquired at each individual electrode, either in time, frequency, or time-frequency domain [9, 10]. An alternative class of methods aim at extracting spatial features as manifested in multichannel EEG signals [11-15]. Adaptive classifiers, matrix and tensor classifiers, transfer learning, and deep learning are among other methods that have more recently been proposed [7, 16, 17].

Graph signal processing (GSP) [18-21] is an emerging field that has attracted great interest. It has in particular been adopted in an increasing number of neuroimaging studies. In [22], insights provided by the GSP perspective for analysis of brain activity using functional magnetic resonance imaging (fMRI) and diffusion-weighted MRI (dMRI) data are presented. In [23], seven different graphs are constructed based on structural and functional connectivity between brain areas to evaluate the benefit of GSP for classification and dimensionality reduction of fMRI data. In [24-26], GSP is used to perform anatomically-informed spatial processing of fMRI data to enhance brain activation mapping. In [27], GSP is leveraged to introduce a measure of the coupling strength between brain structure and function, which has been used within the context of task decoding and individual fingerprinting for fMRI data [28]. In [29], GSP is used to predict autism spectrum disorder from resting-state fMRI data. In [30], by using a multi-modal imaging dataset consisting of EEG, MRI, and dMRI data, the role of structural connectivity in the representation of brain activity signals and their dynamics is explored in a GSP setting. A GSP-based method for feature extraction in near-infrared spectroscopy (NIRS)-based BCI is presented in [31] that captures the spatial information of the NIRS signals.

A number of studies have also shown promising results in applying GSP techniques in classification, dimensionality reduction, and denoising of EEG signals [32-37]. In [32], network harmonics of the brain structural connectivity graph are derived for tracking fast spatiotemporal cortical dynamics. In [33], a dimensionality reduction method for MI-BCI application is proposed via spectral graph decomposition of a brain structural graph. In [34], a GSP-based approach is presented for adaptive dimensionality reduction and classification of MI tasks exploiting geometrical and

Maliheh Miri, Vahid Abootalebi, and Hamid Saeedi-Sourck are with the Department of Electrical Engineering, Yazd University, Yazd, Iran.

Hamid Behjat is with the Department of Biomedical Engineering, Lund University, Lund, Sweden.

corresponding author's e-mail: abootalebi@yazd.ac.ir

correlation graphs of the brain. In [35], GSP techniques are used for emotion recognition using EEG data. In [36], a graph Laplacian denoising method is proposed which improves the separation of MI and resting mental states in MI-BCI EEG data. In [37], an MI decoding approach is proposed that utilizes graph Slepian functions [38], using which discriminative features for classification are extracted from a structural sub-graph of the brain. Inspired by the promising results of the use of GSP in brain imaging applications, we propose a GSP-based method for classification of MI EEG data. Despite the benefits of GSP, its successful application heavily relies on using a suitable graph that can capture subtle intrinsic relations between the data elements. This is not readily available in many applications, such as for EEG data for which, although there is exist a clear definition of graph vertices, there exists no gold standard definition of graph edges and edge weights. In the absence of a well-defined graph, given an ensemble set of signals, graph learning (GL) techniques can be employed to learn a graph from the data at hand. Different GL methods have been proposed in the literature [39]. Here we employ a sub-category of GL that leverages GSP and imposes constraints on graph sparsity and smoothness of graph signal on the resulting graph [40-42].

The method proposed in this paper for EEG data classification is comprised of four stages. First, we use graph learning to learn subject-specific brain graphs; a conventional graph that uses Pearson correlation coefficients as the weight of the edges is also used for comparison. Second, by interpreting EEG data as graph signals, we transform them into the spectral domain of each graph. Third, we derive a discriminative spectral graph subspace that specifically aims at differentiating two-class data. Fourth, we use the extracted features for training and testing a binary classifier.

The remainder of this paper is structured as follows. Section 2 gives an overview of the fundamental concepts. A description of the proposed framework is presented in section 3. Section 4 describes the experimental results and provides a discussion. Finally, section 5 presents our concluding remarks.

II. Materials and Methods

A. Dataset

To evaluate the proposed method, EEG data from the publicly available BCI Competition III-Dataset IVa [43] were used. The data, comprising of two classes of motor imagery EEG signals, were recorded from five healthy subjects (labeled as *aa*, *al*, *av*, *aw*, and *ay*) using 118 electrodes that were installed with the electrode arrangement in the extended international 10/20-system at a sampling rate of 100 Hz. A total of 280 visual cues of length 3.5 seconds were presented to subjects, interleaved with rest interval of random lengths 1.75 to 2.25 seconds. Despite the limited number of subjects, the dataset is rich in the sense that it includes a lot of trials per subject, making it very suitable for use within a machine learning setting, and that it has been utilized in many studies.

During the presentation of target cues, subjects were asked to perform right hand or right foot motor imageries, and 140 trials were acquired for each class. According to the competition instructions the trials were divided into training and test sets in each class, wherein the set sizes differed across the five subjects. More precisely, for the first two subjects most trials are labeled (60% and 80%, respectively), while for the other three 30%, 20%, and 10% labeled trials are given, respectively, and the remaining trials composing their test sets (for more details, see http://www.bbci.de/competition/iii/). As such, performing classification is more challenging on subjects *av*, *aw*, and *ay* due to their small training set size. In this work, a GSP-based approach is provided to tackle the problem of MI tasks classification in this dataset. In the following section, the principles of GSP are briefly reviewed.

B. Graph Signal Processing Fundamentals

Let G = (V, E, $\mathbf{A}$) denote a weighted, undirected graph, where V = {1, 2,…, *N*} represents the graph's finite set of *N* vertices (nodes), E denotes the graph's edge set, i.e., pairs (*i*, *j*) where *i*, *j* ∈ V, and $\mathbf{A}$ is a symmetric matrix ($\mathbf{A}_{i,j} = \mathbf{A}_{j,i}$) that denotes the graph's weighted adjacency matrix. The weights in the adjacency matrix indicate the strength of the connection, or similarity between two corresponding vertices, therefore, $\mathbf{A}_{i,j} = 0$, if there is no connection/similarity between vertices *i* and *j*. Moreover, it is assumed that there are no self-loops in the graph, which implies $\mathbf{A}_{i,i} = 0$. Let ℓ^2(G) denotes the Hilbert space of all square-summable real vectors $\mathbf{f} \in \mathbb{R}^N$, with the inner product defined as $\langle \mathbf{f}_1, \mathbf{f}_2 \rangle = \sum_{k=1}^{N} \mathbf{f}_1[k]\mathbf{f}_2[k]$, and the l_2-norm defined as $\|\mathbf{f}\|^2 = \langle \mathbf{f}, \mathbf{f} \rangle = \sum_{k=1}^{N} |\mathbf{f}[k]|^2$.

A real signal defined on the vertices of G, $\mathbf{f}: \mathrm{V} \rightarrow \mathbb{R}$, can be thus seen as vector in ℓ^2(G), whose *n*-th component represents the signal value at the *n*-th vertex of G. The graph's normalized Laplacian matrix is defined as $\mathbf{L} = \mathbf{I} - \mathbf{D}^{-1/2}\mathbf{A}\mathbf{D}^{-1/2}$, where $\mathbf{I}$ is the identity matrix and $\mathbf{D}$ is the diagonal matrix of vertex degrees, i.e., $\mathbf{D}_{i,i} = \sum_j \mathbf{A}_{i,j}$. Since $\mathbf{L}$ is real, symmetric, and positive semi-definite, it can be diagonalized via eigenvalue decomposition as:

$$\mathbf{L} = \mathbf{U}\mathbf{\Lambda}\mathbf{U}^T, \tag{1}$$

where *T* denotes the transpose operator, $\mathbf{U} = [\mathbf{u}_1, \mathbf{u}_2, ..., \mathbf{u}_N]$ is an orthonormal matrix concatenating the eigenvectors $\mathbf{u}_k \in \ell^2$(G) in its columns, and $\mathbf{\Lambda}$ is a diagonal matrix that stores the corresponding real, and non-negative eigenvalues $0 = \lambda_1 \leq \lambda_2 \leq ... \leq \lambda_N \leq 2$. The eigenvalues define the graph Laplacian spectrum, and the corresponding eigenvectors form an orthonormal basis that spans ℓ^2(G). By using the Laplacian eigenvectors, a graph signal $\mathbf{f}$ can be transformed into a spectral representation, commonly referred to as the graph Fourier transform (GFT) of $\mathbf{f}$, denoted $\hat{\mathbf{f}}$, obtained as:

$$\hat{\mathbf{f}} = \mathbf{U}^T \mathbf{f}. \quad (2)$$

Given the orthonormality of the Laplacian eigenvectors, the inverse GFT of $\hat{\mathbf{f}}$ is obtained as $\mathbf{f} = \mathbf{U}\hat{\mathbf{f}} = \sum_{k=1}^{N} \hat{\mathbf{f}}[k]\mathbf{u}_k$. By synthesizing $\mathbf{f}$ as a weighted sum of orthogonal graph frequency components $\mathbf{u}_k$, the GFT coefficients of $\mathbf{f}$ entail the degree of signal variability of $\mathbf{f}$ over G. That is, each GFT coefficient represents the contribution of its corresponding graph Laplacian eigenvector to the graph signal $\mathbf{f}$. Importantly, the GFT satisfies Parseval's energy conservation relation, i.e., $\|\mathbf{f}\|^2 = \|\hat{\mathbf{f}}\|^2$.

Graph Laplacian eigenvectors associated to larger eigenvalues entail a larger extent of variability, and as such, eigenvalues of the graph Laplacian matrix can be seen as an extension of frequency elements that define the Fourier domain in classical signal processing. To further illustrate the notion of frequency for graph signals, the total variation (TV) of a graph signal $\mathbf{f}$ on graph G can be quantified as:

$$\mathrm{TV}(\mathbf{f}) = \mathbf{f}^T \mathbf{L}\mathbf{f} = \sum_{(i,j)\in E} \mathbf{A}_{i,j} \left(\frac{\mathbf{f}[i]}{\sqrt{\mathbf{D}_{i,i}}} - \frac{\mathbf{f}[j]}{\sqrt{\mathbf{D}_{j,j}}} \right)^2 = \sum_{k=1}^{N} \lambda_k \hat{\mathbf{f}}[k]^2, \quad (3)$$

where larger values of $\mathrm{TV}(\mathbf{f})$ indicate greater changes of $\mathbf{f}$ on G, i.e., higher spatial variability. By viewing each graph Laplacian eigenvector as a graph signal, it can be seen that its total variation is equal to its corresponding eigenvalue, i.e.: $\mathrm{TV}(\mathbf{u}_k) = \mathbf{u}_k^T \mathbf{L}\mathbf{u}_k = \lambda_k$. This relation shows that each eigenvalue is a quantification of the extent of variability of its corresponding eigenvector. Specifically, the graph Laplacian eigenvalues can be seen as graph frequencies, indicating how the eigenvectors vary with respect to the graph G [18, 19]. Graph signal $\mathbf{f}$ is smooth on G if its elements associated to vertices connected via large edge weights have similar values. $\mathrm{TV}(\mathbf{f})$ is a quantification of the extent of variation of $\mathbf{f}$ with respect to the structure of G, thus, providing a measure of the degree of smoothness of $\mathbf{f}$. A leading paradigm in graph learning exploits this notion of smoothness to learn a graph structure on which data comprise certain regularity.

C. *Learning Graphs from Smooth Signals*

A class of GL methods enforce data smoothness, deriving a graph Laplacian matrix via solving [41]:

$$\begin{aligned} &\min_{\mathbf{L}} \quad \mathrm{trace}(\mathbf{F}^T \mathbf{L}\mathbf{F}) + \alpha \|\mathbf{L}\|_F^2, \\ &\text{s.t.} \quad \mathrm{trace}(\mathbf{L}) = N, \quad \mathbf{L}_{i,j} = \mathbf{L}_{j,i} \le 0 \;\; i \ne j, \quad \mathbf{L}\mathbf{1} = \mathbf{0}, \end{aligned} \quad (4)$$

where $\mathbf{F}$ is an $N \times T$ matrix of graph signals, α is regularization parameter, $\|\cdot\|_F$ denotes the Frobenius norm and $\mathbf{1} = [1,...,1]^T$. Minimizing the first term in the objective function guarantees smoothness of the signals on the learned graph, which can be seen via invoking (3): $\mathrm{trace}(\mathbf{F}^T \mathbf{L}\mathbf{F}) = \sum_{t=1}^{T} \mathbf{f}_t^T \mathbf{L}\mathbf{f}_t = \sum_{t=1}^{T} \mathrm{TV}(\mathbf{f}_t)$. The Frobenius norm controls sparsity by shrinking edge weights. The imposed constraints ensure finding a valid Laplacian matrix. Considering $\|\mathbf{L}\|_F^2 = \|\mathbf{A}\mathbf{1}\|^2 + \|\mathbf{A}\|_F^2$, where $\mathbf{A}\mathbf{1}$ denotes the vertices degree vector, the optimization in (4) can be solved more efficiently via a more general-purpose formulation with respect to the graph's weighted adjacency matrix [42]:

$$\begin{aligned} &\min_{\mathbf{A}} \quad \|\mathbf{A} \circ \mathbf{Z}\|_1 + \alpha \|\mathbf{A}\mathbf{1}\|^2 + \alpha \|\mathbf{A}\|_F^2, \\ &\text{s.t.} \quad \mathrm{diag}(\mathbf{A}) = \mathbf{0}, \quad \mathbf{A}_{i,j} = \mathbf{A}_{j,i} \ge 0 \;\; i \ne j, \end{aligned} \quad (5)$$

where $\mathbf{Z}$ denotes the pairwise Euclidean distance matrix of the signals residing on the graph vertices, with entries given as $\mathbf{Z}_{i,j} = \|\mathbf{x}_i - \mathbf{x}_j\|^2$, where $\mathbf{x}_i \in \mathbb{R}^T$ denotes the signal vector residing on vertex *i*. The first term in this objective function finds the graph's adjacency matrix under the smoothness assumption; note the equivalence between the first terms in (4) and (5), i.e., $\mathrm{trace}(\mathbf{F}^T \mathbf{L}\mathbf{F}) = 0.5\|\mathbf{A} \circ \mathbf{Z}\|_1$, where $\circ$ is the Hadamard product. Intuitively, if smooth graph signals reside on well-connected vertices (i.e. vertices connected via large weight edges), it is expected that these vertices have smaller distances $\mathbf{Z}_{i,j}$. Alternatively, the objective function (5) can be improved by replacing the l_2-norm with a logarithmic barrier on the vertices degree vector as:

$$\begin{aligned} &\min_{\mathbf{A}} \quad \|\mathbf{A} \circ \mathbf{Z}\|_1 - \alpha \mathbf{1}^T \log(\mathbf{A}\mathbf{1}) + \frac{\beta}{2} \|\mathbf{A}\|_F^2, \\ &\text{s.t.} \quad \mathrm{diag}(\mathbf{A}) = \mathbf{0}, \quad \mathbf{A}_{i,j} = \mathbf{A}_{j,i} \ge 0 \;\; i \ne j, \end{aligned} \quad (6)$$

where the second term ensures graph degrees to be positive, thus improving the overall connectivity of the graph, and moreover, ensures each vertex having at least one edge. α and β are regularization parameters, and the constraints guarantee to obtain a valid adjacency matrix. The third term controls the sparsity of the resulting graph; intuitively, smaller values of β yield sparser graphs by penalizing edges between vertices with larger $\mathbf{Z}_{i,j}$ [42]. In the following, we refer to the GL approaches given in (5) and (6) as the *l_2-penalized* and *log-penalized* methods, respectively.

D. *Two-Class Discriminative Subspace via Simultaneous Diagonalization of Covariance Matrices*

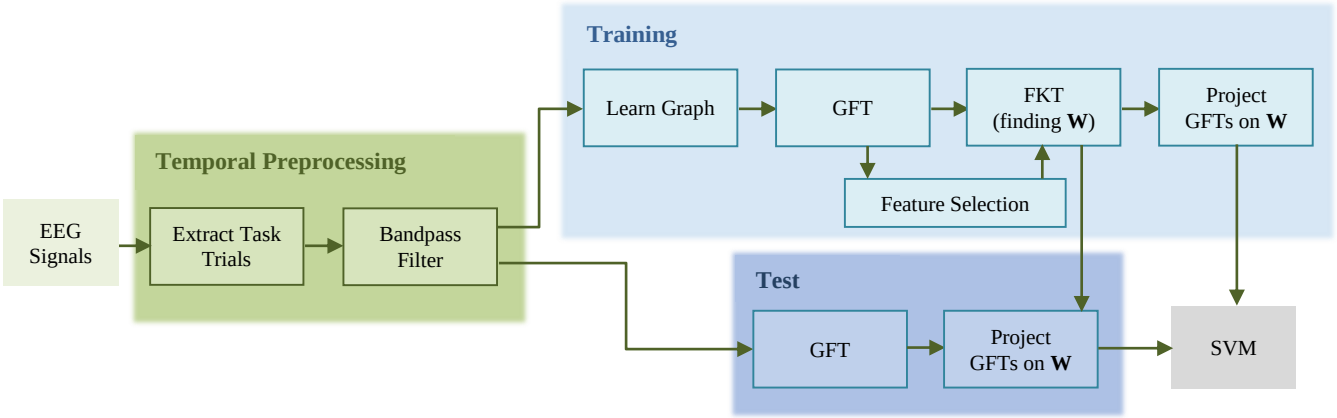

Fig. 1. A schematic overview of the proposed method.

After defining a brain graph, the graph spectral representations of the EEG signals were considered to find a discriminative subspace for two-class (right hand and right foot) MI classification. To this end, inspired by the Fukunaga-Koontz transform (FKT) [44], and the method presented in [29], simultaneous diagonalization of two covariance matrices was utilized. For graph signal $\mathbf{f}$ defined on G, let $\tilde{\mathbf{f}}$ denote the de-meaned and normalized version of $\mathbf{f}$ obtained as [45]:

$$\tilde{\mathbf{f}} = (\mathbf{f} - \mathbf{u}_1^T \mathbf{f}\, \mathbf{u}_1) \Big/ \left\| \mathbf{f} - \mathbf{u}_1^T \mathbf{f}\, \mathbf{u}_1 \right\|^2 . \tag{7}$$

Let $\mathbf{F}$ denote an $N \times T$ matrix that contains a single trial of the EEG time series, with $\mathbf{F}_{c,t}$ being the signal value at electrode *c* at time point *t*, and let $\hat{\tilde{\mathbf{F}}}$ denote the GFT matrix of the de-meaned and normalized trial. The goal is to determine a projection matrix $\mathbf{W}$ that simultaneously diagonalizes:

$$\mathbf{\Sigma} = \mathbf{\Sigma}_1 + \mathbf{\Sigma}_2, \quad \mathbf{\Sigma}_i = \mathbf{C}_i / \operatorname{trace}(\mathbf{C}_i), \quad \mathbf{C}_i = \hat{\tilde{\mathbf{F}}}_i \hat{\tilde{\mathbf{F}}}_i^T , \tag{8}$$

where $\mathbf{\Sigma}_1$ and $\mathbf{\Sigma}_2$ denote the ensemble averaged covariance matrices of the trials in class 1 (right hand) and class 2 (right foot), respectively. As $\mathbf{\Sigma}$ is positive definite, it can be eigen-decomposed, $\mathbf{\Sigma} = \mathbf{V} \mathbf{\Gamma} \mathbf{V}^T$, where $\mathbf{V}$ is the matrix of eigenvectors of $\mathbf{\Sigma}$ and $\mathbf{\Gamma}$ is the diagonal matrix of the corresponding eigenvalues; using which a whitening transform $\mathbf{P}$ can be obtained as:

$$\mathbf{P} = \mathbf{\Gamma}^{-1/2} \mathbf{V}^T . \tag{9}$$

By whitening $\mathbf{\Sigma}$ with $\mathbf{P}$, the variances in the space spanned by $\mathbf{V}$ will become equal, resulting in all the eigenvalues becoming equal to one, i.e.:

$$\mathbf{P} \mathbf{\Sigma} \mathbf{P}^T = \mathbf{P}(\mathbf{\Sigma}_1 + \mathbf{\Sigma}_2)\mathbf{P}^T = \mathbf{S}_1 + \mathbf{S}_2 = \mathbf{I}. \tag{10}$$

Consequently, eigenvalue decomposition of $\mathbf{S}_1$ and $\mathbf{S}_2$ gives:

$$\mathbf{S}_1 = \mathbf{B} \mathbf{\Gamma}_1 \mathbf{B}^T , \quad \mathbf{S}_2 = \mathbf{B}(\mathbf{I} - \mathbf{\Gamma}_1)\mathbf{B}^T , \tag{11}$$

where $\mathbf{B}$ denotes the eigenvectors, which are the same for both $\mathbf{S}_1$ and $\mathbf{S}_2$, and their corresponding eigenvalues are complementary; i.e., by sorting the eigenvalues in descending order, the eigenvector associated with the largest eigenvalue of $\mathbf{S}_1$ is associated with the smallest eigenvalue of $\mathbf{S}_2$. Therefore, a small combination of the first and last eigenvectors of $\mathbf{B}$ induces a suitable discriminatory transform for differentiating the two classes. Finally, the overall projection matrix can be obtained as $\mathbf{W} = \mathbf{B}^T \mathbf{P}$.

By applying $\mathbf{W}$ to the GFT coefficients, i.e. $\mathbf{y} = \mathbf{W}\hat{\tilde{\mathbf{f}}}$, we obtained a feature vector $\mathbf{y}$, the variance of which is maximized in one class while minimized in the other class. These features were then used for classification.

III. Proposed Method

The proposed method for EEG-based MI task decoding is illustrated as a block diagram in Fig. 1. The training and test EEG signal sets for each subject are initially preprocessed, and then fed into the training and test phases, respectively. As temporal preprocessing, for each trial, we used the time points within the 0.5-2.5 second interval after the visual cue to construct graph signals; this 2-second interval has been previously used in related works [13, 15, 37]. Motor activity, be it real or imagined, modulates the mu and beta rhythms, therefore, we filtered the extracted signal with a third-order Butterworth filter with a passband of 8-30 Hz. Graph signals were then extracted from these filtered signals; in particular, we defined one graph signal per time instance, i.e., each signal represents EEG values across the 118 electrodes, which, thus, resulted in T=200 graph signals per trial.

A. Graph-based Representation of Brain Signals

In the training phase, we modeled the structure of the brain of each subject as a graph, in which vertices corresponded to the EEG electrodes and edges were defined by estimating the graph's weighted adjacency matrix using the log-penalized and l_2-penalized graph learning frameworks. As a means of

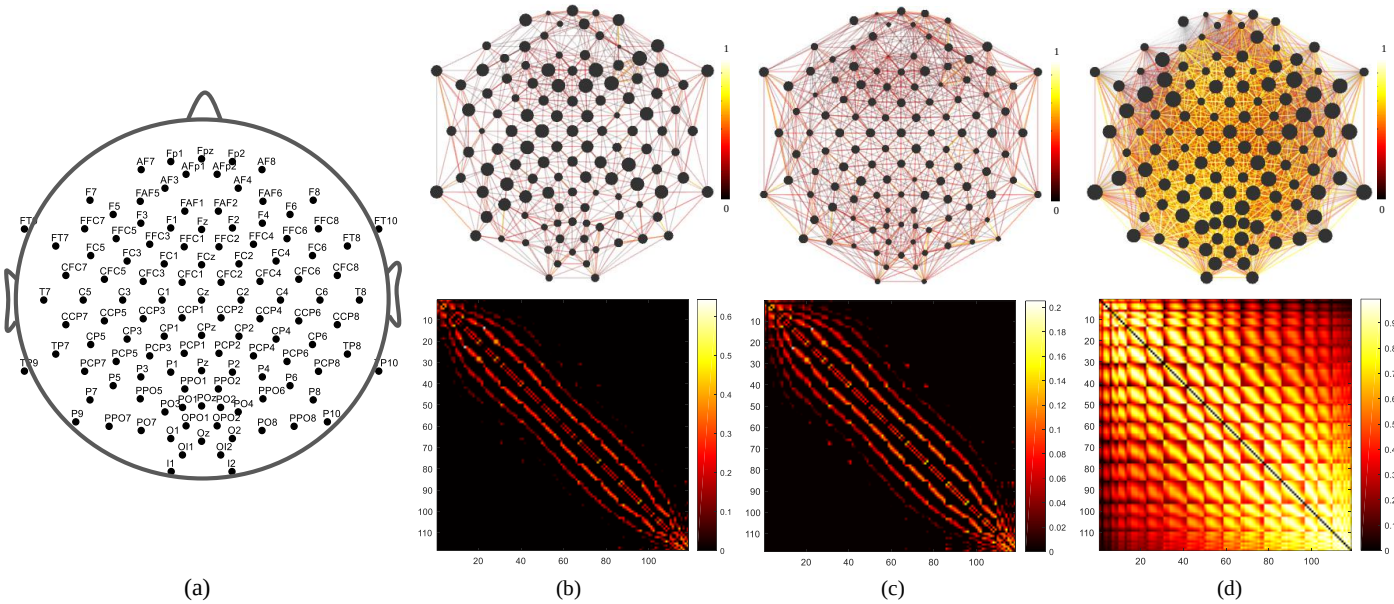

(a) (b) (c) (d)

Fig. 2. (a) Arrangement of EEG electrodes. (b, c, d) log-penalized, l_2-penalized, and correlation graphs with their related adjacency matrices for subject *aa*, respectively. Edge widths and colors reflect edge weights, and vertex sizes reflect nodal degrees. For better visualization, only the top 50% of edges that have the largest weights are shown in the correlation graph. The graphs were plotted by modifying the base code provided in GSPbox [47].

comparison, we also defined a fully connected correlation graph in which edge weights were defined based on the degree of functional connectivity between electrode pairs; that is, for each electrode pair, the absolute value of the Pearson correlation coefficient between their time courses was defined as the edge weight, reflecting an estimate of the overall statistical dependency between the two electrodes [46].

For each graph, the eigenvectors of $\mathbf{L}$ were used to compute the GFT of each graph signal. Using FKT, a transformation matrix $\mathbf{W}$ that maps the GFT coefficients into a discriminative graph spectral subspace was then derived. The mapped data were then treated as discriminative features. To determine the most effective graph frequency harmonics for classifying the EEG signals, a feature selection algorithm was used; we ranked the GFT coefficients based on their energy using MATLAB's `rankfeatures` function that utilizes the Wilcoxon statistical test. GFT Coefficients with higher ranks correspond to more distinctive features. The number of selected features for each subject was determined using 10-fold cross-validation.

B. Evaluation

The classifier was trained using labelled training data, where labels indicate the class of each trial, and classification performance was evaluated with the labelled test data. The projection matrix $\mathbf{W}$ and the index of discriminative GFT features were computed in the training phase and consequently used in the test phase. The logarithm of variance of the projected GFT coefficients on $\mathbf{W}$ were used as features to train a support vector machine (SVM) classifier with a linear kernel. Since this projection maximizes the variance of the signals from one class while minimizing it for the signals from the other class, it provides discriminative features for classification. We used SVM due to its overall superior robustness and efficiency in the BCI applications compared to other classifiers [7]. The linear kernel was selected for its simplicity and low computational cost.

IV. RESULTS AND DISCUSSION

Fig. 2(a) shows the arrangement of the 118 electrodes on the head. Fig. 2(b-d) shows the three brain graphs and their corresponding adjacency matrices for subject *aa*. The nodal degrees are comparable between the learned graphs but are differently scaled for the correlation graph due to the large difference between the degree distributions. The correlation graph is fully connected as it is defined based on the correlation of all electrode pairs, whereas the two learned graphs are notably sparse, a result of sparsity-inducing terms used in the learning process. The log-penalized method yields sparser learned graphs compared to the l_2-penalized method. For log-penalized, l_2-penalized and correlation graphs, on average across subjects, the number of edges were 1684.8±367.9, 2519.2±366.9, and 13806, respectively; additional quantitative comparison of the graphs is presented in the supplementary material. The sparsity of graphs is desirable because it plays a key role in reducing the computational burden of algorithms and makes them suitable for online BCI applications. Graphs constructed for the other four subjects are shown in Fig. S2 in the supplementary material.

Distribution and histogram of the normalized Laplacian eigenvalues for three graphs of subject *aa* are shown in Fig. 3(a). Most of the eigenvalues in the correlation graph are concentrated around one, whereas the eigenvalues of the learned graphs, especially the log-penalized graph, gradually increase, and are more widely distributed along the spectrum. Eigenvalues with high multiplicity around one (a high peak at $\lambda \simeq 1$) in the correlation graph spectrum suggest vertex duplication, in which a new vertex to the graph has an

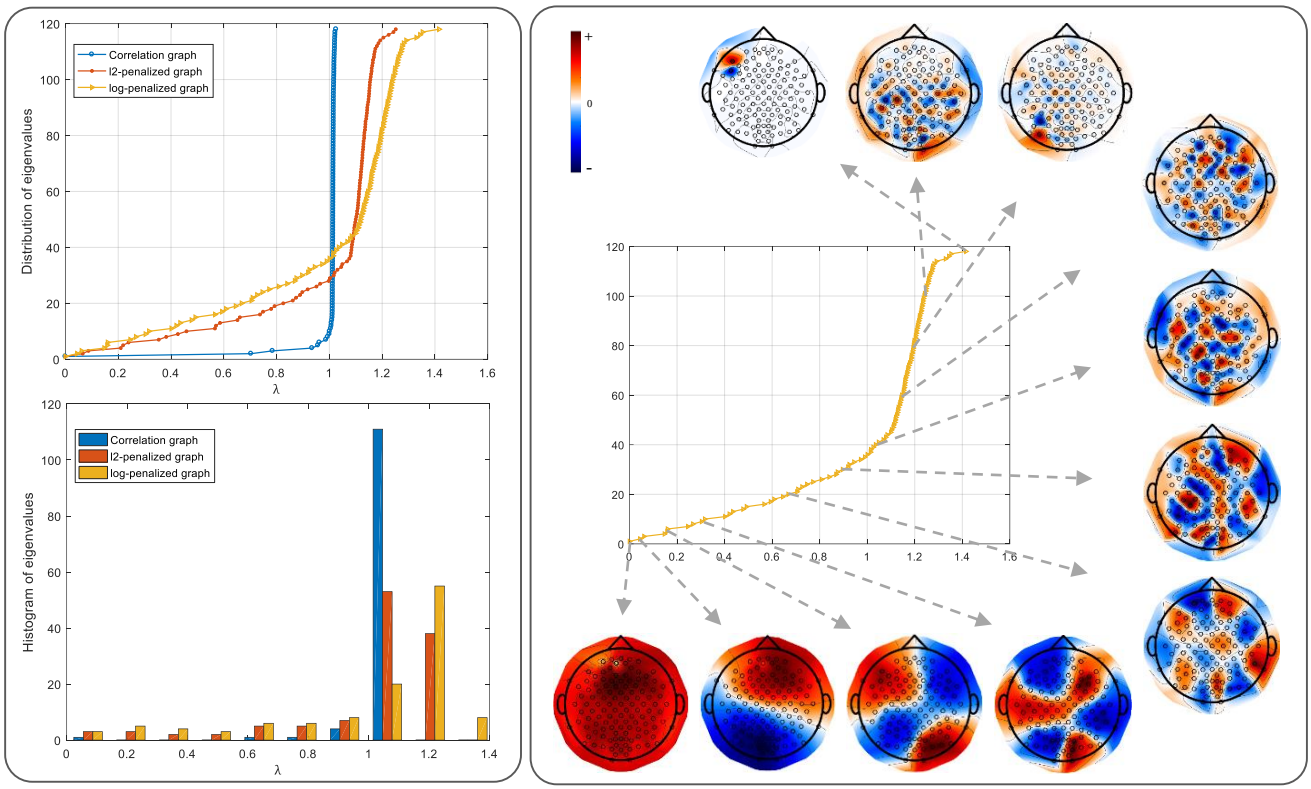

(a) (b)

Fig. 3. a) Distribution and histogram of eigenvalues in the log-penalized, l_2-penalized, and correlation graphs for subject *aa*. b) Eigenvalues and some of the corresponding eigenvectors of the log-penalized graph.

identical connectivity pattern to the duplicated vertex, resulting in vertices with the same connectivity profile [48].

Fig. 3(b) illustrates eigenvectors associated to several of the selected normalized Laplacian eigenvalues of the log-penalized graph. The first eigenvector is almost evenly distributed over all the graph vertices and given that $\mathrm{TV}(\mathbf{u}_1) = \lambda_1 = 0$, there is no notable spatial variation. In the next eigenvectors, the increase in spatial variability is proportional to the increase in graph frequencies. The last eigenvector is highly localized, which is in line with normalized Laplacian matrices characteristics that manifest localized patterns of spatial variability in high frequencies.

Fig. 4 shows several of the eigenvectors and their corresponding eigenvalues for the three studied graphs for subject *aa*. The eigenvectors of the learned graphs capture a wider range of variability compared to the correlation graph, many eigenvectors of which manifest spatial patterns with similar spatial variabilities corresponding to a spectral value around one. This suggests that in the correlation graph most of the vertices are connected to other vertices in a rather similar pattern. Given that graph Laplacian eigenvectors form an orthonormal basis that represent signals, their broader spatial variability with respect to the graph structure can provide a more precise representation of signals. Accordingly, in GFT, a graph signal is mapped to the graph frequency domain using the Laplacian eigenvectors, the spatial variability of which plays an important role in obtaining an effective decomposition. In the correlation graph, a small subset of the first eigenvectors captures a substantial portion of the total signal energy, whereas in the learned graphs, signal energy is distributed across a wider range of eigenvectors. The complete set of eigenvectors of the three studied graphs for subject *aa* are shown in supplementary material Fig. S3.

Alternatively, a weighted measure of the number of zero crossings (WZC) can be used to quantify spatial variability of eigenvectors, or any graph signal in general. Strictly speaking, WZC is a weighted measure of changes in the sign of the eigenvectors at the adjacent graph vertices, wherein the adjacency matrix entries are used as weights, computed as:

$$\mathrm{WZC}(\mathbf{u}_k) = \frac{1}{2} \sum_{(i,j)\in E} \mathbf{A}_{i,j} H(-\mathbf{u}_k[i]\,\mathbf{u}_k[j]), \tag{12}$$

where $H(.)$ is the Heaviside step function. The WZC of the normalized Laplacian eigenvectors of the three studied graphs is shown in Fig. 5. Spatial variability of eigenvectors generally increases by increasing the eigenvalue indices. WZC gradually increases along the spectrum in the learned graphs, especially in the log-penalized one, whereas in the correlation graph, it sharply increases in the initial eigenvalue indices, and then only minimally changes in the remainder of the spectrum. These results corroborate visual interpretations made on spatial variability of eigenvectors as shown in Fig. 4, reflecting the superior capability of the learned graphs over the correlation graph in capturing a wide range of spatially varying pattern as manifested by EEG signals.

In the first experiment, five different sets of the GFT coefficients were utilized. The first set consisted of the entire

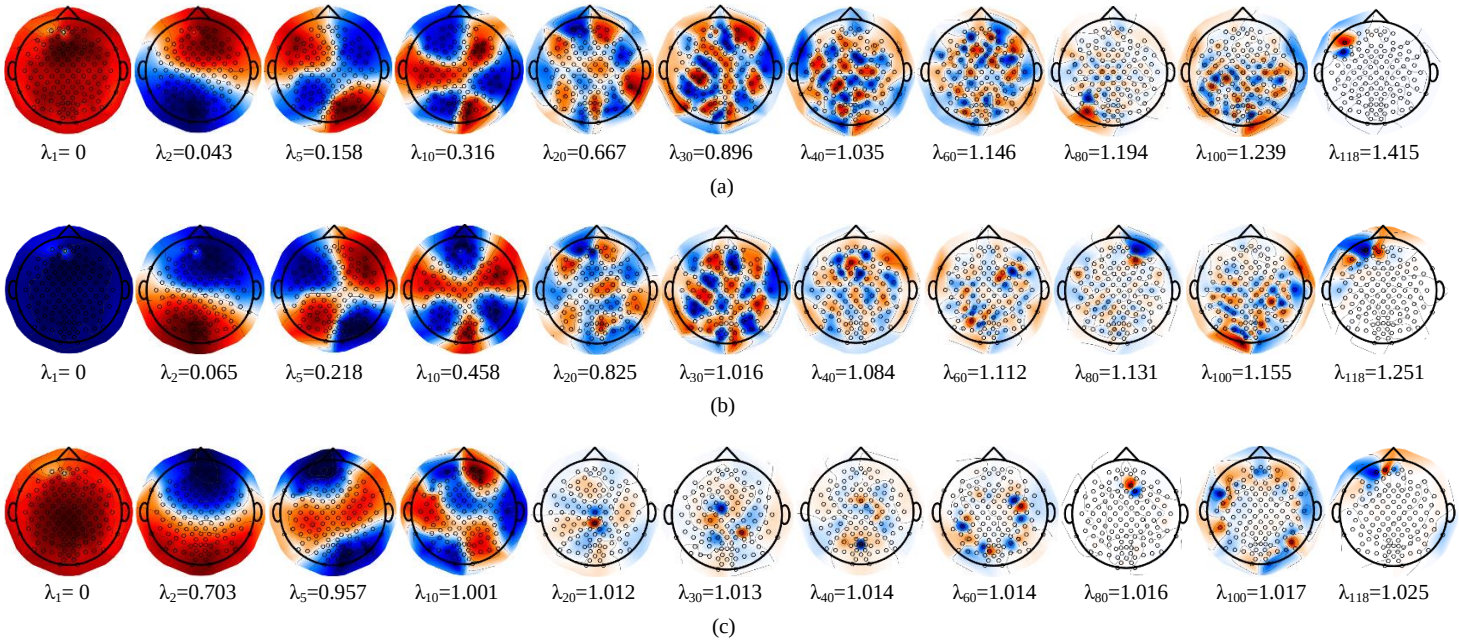

Fig. 4. Some of the selected eigenvectors $\mathbf{u}_k$ (k = 1, 2, 5, 10, 20, 30, 40, 60, 80, 100, 118) of the (a) log-penalized, (b) l_2-penalized, and (c) correlation graphs of subject *aa*, respectively.

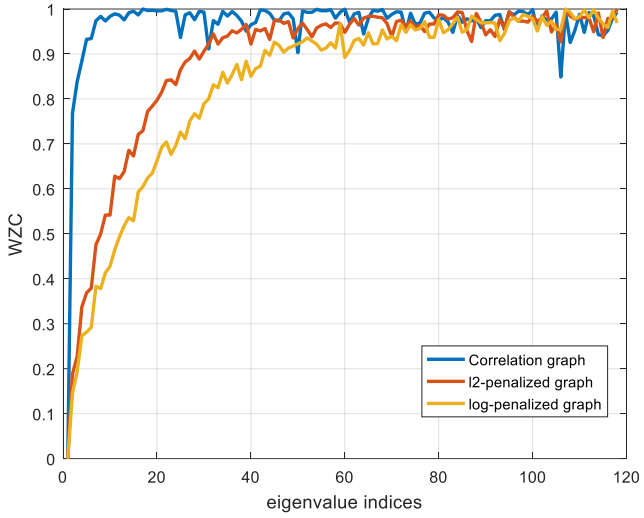

Fig. 5. Weighted zero crossings for the log-penalized, l_2-penalized, and correlation graphs of subject *aa*.

set of GFT coefficients, denoted all frequencies (AF). Inspired by prior works on the application of GFT on brain imaging data [49, 50], three additional sets of GFT coefficients were defined by dividing the spectrum into three equal frequency bands, denoted low (LF), medium (MF) and high (HF) frequencies. Inspired by [36], a fifth subset was defined via the union of the LF and HF subsets, denoted LF+HF. These five sets of GFT coefficients were then used as inputs to the FKT to derive a discriminative matrix $\mathbf{W}$ for each set. Consequently, features for classification were extracted by computing the logarithm of variance of the projected GFT coefficients on $\mathbf{W}$. Table I presents classification accuracies using three different graphs for each individual subject and also on average across subjects.

TABLE I
CLASSIFICATION ACCURACIES (%) ON THE TEST SETS FOR EACH SUBJECT AND ON AVERAGE ACROSS SUBJECTS USING THREE BRAIN GRAPHS AND IN FIVE DIFFERENT FREQUENCY BAND SETTINGS

log-penalized	*aa*	*al*	*av*	*aw*	*ay*	Mean ± std
AF	74.11	100	70.41	90.18	74.21	81.78 ± 12.73
LF	86.61	100	70.92	91.96	84.92	**86.88** ± **10.68**
MF	55.36	66.07	52.55	63.39	54.36	58.35 ± 5.99
HF	51.78	80.36	43.88	59.37	47.22	56.52 ± 14.53
LF+HF	74.11	100	71.43	90.62	75.79	82.39 ± 12.35
l_2-penalized	*aa*	*al*	*av*	*aw*	*ay*	Mean ± std
AF	69.64	100	70.41	89.73	72.22	80.40 ± 13.73
LF	87.5	98.21	70.41	83.03	88.49	**85.53** ± **10.10**
MF	54.46	67.86	53.06	62.05	55.16	58.52 ± 6.27
HF	54.46	80.36	44.39	55.80	51.19	57.24 ± 13.66
LF+HF	78.57	100	72.45	86.61	78.57	83.24 ± 10.63
correlation	*aa*	*al*	*av*	*aw*	*ay*	Mean ± std
AF	70.53	100	70.92	88.39	72.22	80.41 ± 13.25
LF	86.61	100	68.88	94.2	87.7	**87.47** ± **11.71**
MF	52.68	78.57	54.59	54.91	53.97	58.94 ± 11
HF	55.36	71.43	56.12	51.34	48.41	56.53 ± 8.89
LF+HF	66.96	100	71.43	91.96	84.13	82.9 ± 13.8

Using the LF GFT coefficients resulted in substantially higher classification accuracies compared to using the MF, HF or LF+HF components, in all subjects as well as on average across subjects. It also provided higher accuracies compared to using all the GFT coefficients, in subjects *aa*, *aw*, and *ay*. Moreover, the learned graphs achieved better results compared to the correlation graph in three out of five subjects (*aa*, *av*, and *ay*). To determine an optimal subset of the GFT coefficients that provide the most discriminative features for

classification, we implemented feature selection. The logarithm of variance of the GFT coefficients was used as input to feature selection. Fig. 6 illustrates the scores of graph frequencies in the log-penalized graph for each subject and on average across subjects.

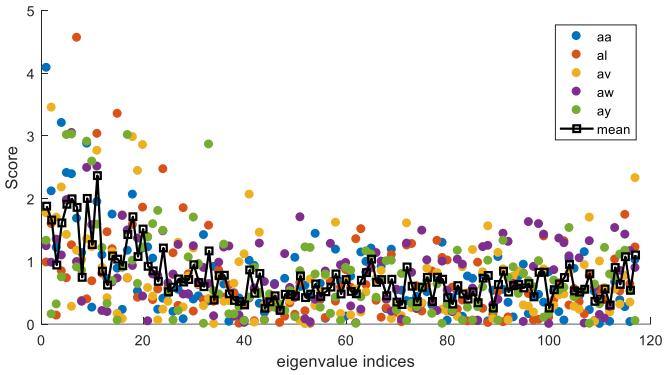

Fig. 6. Scores of the graph frequencies in the proposed log-penalized graph for each individual subject and on average across subjects.

The lowest one-third eigenvalue indices attained substantially higher scores than the rest of the spectrum, corroborating results presented in Table I. Therefore, we only used features from this sub-band as the most effective harmonics for each subject, classification accuracies for which are presented in Table II. To evaluate the effectiveness of using the FKT, results of classification using GFT coefficients (without FKT) are also provided in Table II. The direct use of the GFT coefficients is prone to overfitting due to the small size of the training samples in comparison to the dimension of the feature vectors, especially in the subjects with small training sets. Therefore, a subset of GFT coefficients as determined by the feature selection step were fed into the classifier.

TABLE II
CLASSIFICATION ACCURACIES (%) FOR GFT AND THE PROPOSED METHOD WITH SELECTED FEATURES FROM THE LF SUB-BAND OF GRAPH SPECTRUM

GFT	*aa*	*al*	*av*	*aw*	*ay*	Mean ± std
log-penalized	61.61	87.5	60.71	70.53	81.75	72.42 ± 11.96
l_2-penalized	65.18	91.07	57.65	67.86	66.27	69.61 ± 12.62
correlation	68.75	96.43	62.75	73.21	68.65	73.96 ± 13.1
Proposed	***aa***	***al***	***av***	***aw***	***ay***	**Mean ± std**
log-penalized	87.5	100	70.92	91.96	92.86	**88.65 ± 10.88**
l_2-penalized	87.5	98.21	72.96	84.82	88.49	86.4 ± 9.06
correlation	90.18	100	68.88	94.2	88.89	88.43 ± 11.75

The results suggest that using FKT notably improves the classification accuracies compared to directly using the GFT coefficients. That is, mapping the GFT coefficients onto the subspace provided by FKT results in features that better discriminate the two MI classes. This FKT-based approach of extracting features from a temporal set of GFT coefficients is in contrast to prior related works [22, 27] wherein the temporal mean or variance of the GFT coefficients is considered as feature, which notably discards the temporal dynamics. The temporal evolution of GFT coefficients of two representative EEG trials is shown in Fig. S4 in the supplementary material. Overall, the best average accuracy was obtained in the proposed method by using the log-penalized graph learning approach.

Finally, the performance of the proposed method is compared to three alternative state-of-the-art methods; see Table III. The proposed method using log-penalized graph learning outperforms the three alternative methods, on average across subjects. The GSL method, which is GSP-based [37], shows the best classification accuracy in subject *av*, whereas the RCSSP method, which utilizes an extension of FKT [15], shows the best accuracy in subject *aw*. In the other three subjects, the proposed method yields higher classification accuracy.

TABLE III
COMPARISON OF CLASSIFICATION ACCURACIES (%) FOR THE PROPOSED METHOD AND THREE ALTERNATIVE STATE-OF-THE-ART METHODS

Method	*aa*	*al*	*av*	*aw*	*ay*	Mean ± std
Proposed (log-penalized)	87.5	100	70.92	91.96	92.86	**88.65 ± 10.88**
GSL [37]	85.71	98.21	75	85.27	90.48	86.93 ± 8.46
RCSSP [15]	82.14	96.42	68.87	98.21	88.88	86.91 ± 11.94
l1-CSP [13]	78.57	98.21	54.08	80.35	83.33	78.91 ± 15.6

V. CONCLUSIONS

We proposed a GSP-based method for classification of motor imagery tasks from EEG signals. We treated EEG signals as functions defined on the vertices of three different graphs, in particular, two classes of subject-specific graphs learned from the data. Our analysis showed that imagined motor activities are generally spatially smooth on the learned graphs, and can thus be effectively represented by using only a subset of their graph frequency components. Furthermore, we showed that temporal dynamics manifested in EEG signals can be captured by using the FKT transformation, resulting in a discriminative subspace that can better separate motor imagery classes. The classification results showed the superior performance of the proposed method compared to three prior related alternative methods, indicating the benefit of extracting features via integrating spatial and temporal characteristics of EEG signals within a GSP setting. In future work, to obtain more informative features at the resolution of multiple frequency bands rather than at the resolution of eigenvalues, we will investigate how EEG signals can be best abstracted based on the distribution of their energy in the graph spectral domain using filter banks [45, 51].

ACKNOWLEDGMENT

The authors certify that they have no conflict of interest to report in regards to the subject matter discussed in this paper. The authors are grateful to Itani and Thanou [29] for sharing the code of their paper. A preliminary version of this work has been presented [46].

REFERENCES

[1] P.L. Nunez, and R. Srinivasan. *Electric fields of the brain: the neurophysics of EEG*. Oxford University Press, 2006.

[2] G. Pfurtscheller, and C. Neuper, "Motor imagery and direct brain-computer communication," *Proc. IEEE*, vol. 89, no. 7, pp. 1123–1134, 2001.

[3] D. J. McFarland, *et al.*, "Mu and beta rhythm topographies during motor imagery and actual movements," *Brain Topogr.*, vol. 12, no. 3, pp. 177-186, 2000.

[4] H. Yu, *et al.*, "Effects of motor imagery tasks on brain functional networks based on EEG Mu/Beta rhythm," *Brain Sci.* vol. 12, no. 2, pp. 194, 2022.

[5] F. Lotte, *et al.*, "Electroencephalography (EEG)-based brain-computer interfaces," *Wiley*, pp. 44, 2015.

[6] N. Padfield, *et al.*, "EEG-based brain-computer interfaces using motor-imagery: Techniques and challenges," *Sens.*, vol. 19, no. 6, pp. 1423, 2019.

[7] F. Lotte, *et al.*, "A review of classification algorithms for EEG-based brain–computer interfaces: a 10 year update," *J. neural Eng.*, vol. 15, no. 3, pp. 031005, 2018.

[8] A. Singh, *et al.*, "A comprehensive review on critical issues and possible solutions of motor imagery based electroencephalography brain-computer interface," *Sensors*, vol. 21, no. 6, pp. 2173, 2021.

[9] S. Lee, *et al.*, "Comparative analysis of features extracted from EEG spatial, spectral and temporal domains for binary and multiclass motor imagery classification," *Inf. Sci.*, vol. 502, pp. 190-200, 2019.

[10] C. Kim, *et al.*, "An effective feature extraction method by power spectral density of EEG signal for 2-class motor imagery-based BCI," *Med. Biol. Eng. Comput.*, vol. 56, no. 9, pp. 1645-1658, 2018.

[11] H. Ramoser, *et al.*, "Optimal spatial filtering of single trial EEG during imagined hand movement," *IEEE Trans. Rehabil. Eng.*, vol. 8, no. 4, pp. 441–446, 2000.

[12] F. Lotte, and C. Guan, "Regularizing common spatial patterns to improve BCI designs: Unified theory and new algorithms," *IEEE Trans. Biomed. Eng.*, vol. 58, no. 2, pp. 355-362, 2011.

[13] B. Wang, *et al.*, "Common spatial pattern reformulated for regularizations in brain–computer interfaces," *IEEE Trans. Cybern.*, vol. 51, no. 10, pp. 5008-5020, 2020.

[14] B. Chakraborty, *et al.*, "Designing phase-sensitive common spatial pattern filter to improve brain-computer interfacing," *IEEE Trans. Biomed. Eng.*, vol. 67, no. 7, pp. 2064-2072, 2020.

[15] M.N Cherloo, *et al.*, "Ensemble regularized common spatio-spectral pattern (ensemble RCSSP) model for motor imagery-based EEG signal classification," *Comput. Biol. Med.*, pp.104546, 2021.

[16] V. Peterson, *et al.*, "Transfer learning based on optimal transport for motor imagery brain-computer interfaces," *IEEE Trans. Biomed. Eng.*, vol. 69, no. 2, pp. 807-817, 2022.

[17] P. Autthasan *et al.*, "MIN2Net: end-to-end multi-task learning for subject-independent motor imagery EEG classification," *IEEE Trans. Biomed. Eng.*, vol. 69, no. 6, pp. 2105-2118, 2022.

[18] D.I. Shuman, *et al.*, "The emerging field of signal processing on graphs: Extending high-dimensional data analysis to networks and other irregular domains," *IEEE Signal Process. Mag.*, vol. 30, no. 3, pp. 83–98, 2013.

[19] A. Ortega, *et al.*, "Graph signal processing: Overview, challenges, and applications," *Proc. IEEE*, vol. 106, no. 5. pp. 808–828, 2018.

[20] D.I. Shuman, *et al.*, "Vertex-frequency analysis on graphs," *Appl. Comput. Harmon. Anal.*, vol. 40, no. 2, pp. 260-291. 2016.

[21] L. Stanković, *et al.*, "Vertex-frequency graph signal processing: A comprehensive review," *Digital Signal Process.*, pp. 102802, 2020.

[22] W. Huang, *et al.*, "A graph signal processing perspective on functional brain imaging," *Proc. IEEE*, vol. 106, no. 5, pp. 868-885, 2018.

[23] M. M´enoret, *et al.*, "Evaluating graph signal processing for neuroimaging through classification and dimensionality reduction," *IEEE Conf. Signal Inf. Process. (GlobalSIP)*, 2017, pp. 618–622.

[24] H. Behjat, *et al.*, "Anatomically-adapted graph wavelets for improved group-level fMRI activation mapping," *NeuroImage*, vol. 123, pp. 185-199, 2015.

[25] D. Abramian, *et al.*, "Diffusion-informed spatial smoothing of fMRI data in white matter using spectral graph filters," *Neuroimage*, vol. 237, pp. 118095, 2021.

[26] H. Behjat, *et al.*, "Cortical surface-informed volumetric spatial smoothing of fMRI data via graph signal processing," *IEEE Int. Conf. Eng. Med. Biol. Soc. (EMBC)*, 2021, pp. 3804-3808.

[27] M.G. Preti, and D. Van De Ville, "Decoupling of brain function from structure reveals regional behavioral specialization in humans," *Nat. commun.*, vol. 10, no. 1, pp. 1-7, 2019.

[28] A. Griffa, *et al.*, "Brain structure-function coupling provides signatures for task decoding and individual fingerprinting," *NeuroImage*, vol. 250, pp. 118970, 2022.

[29] S. Itani, and D. Thanou, "Combining anatomical and functional networks for neuropathology identification: A case study on autism spectrum disorder," *Med. Image Anal.*, vol. 69, pp.101986, 2021.

[30] J. Rué-Queralt, *et al.*, "The connectome spectrum as a canonical basis for a sparse representation of fast brain activity," *NeuroImage*, vol. 244, pp. 118611, 2021.

[31] P.C. Petrantonakis, and I. Kompatsiaris, "Single-trial NIRS data classification for brain–computer interfaces using graph signal processing," *IEEE Trans. Neural Syst. Rehabil. Eng.*, vol. 26, no. 9, pp. 1700-1709, 2018.

[32] K. Glomb, *et al.*, "Connectome spectral analysis to track EEG task dynamics on a subsecond scale," *NeuroImage*, vol. 221, pp. 117137, 2020.

[33] T. Tanaka, *et al.*, "Dimensionality reduction of sample covariance matrices by graph Fourier transform for motor imagery brain-machine interface," *IEEE Stat. Signal Process. WKSH (SSP)*, 2016, pp. 1-5.

[34] G. Kalantar, *et al.*, "Adaptive dimensionality reduction method using graph-based spectral decomposition for motor imagery-based brain-computer interfaces," *Proc. IEEE Global Conf. Signal Inf. Process. (GlobalSIP)*, 2017, pp. 990–994.

[35] S.S. Saboksayr, *et al.*, "EEG-based emotion classification using graph signal processing," *IEEE Int. Conf. Acoustics, Speech Signal Process. (ICASSP)*, 2021, pp. 1065-1069.

[36] T. Cattai, *et al.*, "Improving J-divergence of brain connectivity states by graph Laplacian denoising," *IEEE Trans. Signal Inf. Process. Networks*, vol.7, pp. 493-508, 2021.

[37] K. Georgiadis, *et al.*, "Covariation informed graph slepians for motor imagery decoding," *IEEE Trans. Neural Syst. Rehabil. Eng.*, vol. 29, pp. 340-349, 2021.

[38] D. Van De Ville, *et al.*, "When slepian meets fiedler: Putting a focus on the graph spectrum," *IEEE Signal Process. Lett.*, vol. 24, no. 7, pp. 1001–1004, 2017.

[39] F. Xia, *et al.*, "Graph learning: A survey," *IEEE Trans. Artif. Intell.*, no. 2, pp. 109-127, 2021.

[40] G. Mateos, *et al.*, "Connecting the dots: Identifying network structure via graph signal processing," *IEEE Signal Process. Mag.*, vol. 36, no. 3, pp. 16–43, 2019.

[41] X. Dong, *et al.*, "Learning Laplacian matrix in smooth graph signal representations," *IEEE Trans. Signal Process.*, vol. 64, no. 23, pp. 6160–6173, 2016.

[42] V. Kalofolias, "How to learn a graph from smooth signals," *Artif. Intell. and Stat.*, PMLR, pp. 920-929, 2016.

[43] B. Blankertz, *et al.*, "The BCI competition III: Validating alternative approaches to actual BCI problems," *IEEE Trans. Neural Syst. Rehabil. Eng.*, vol. 14, no. 2, pp. 153–159, 2006.

[44] K. Fukunaga, *Introduction to Statistical Pattern Recognition*. New York, Academic Press, 1990, second edition.

[45] H. Behjat, and M. Larsson, "Spectral characterization of functional MRI data on voxel-resolution cortical graphs," *IEEE Int. Symp. Biomed. Imaging (ISBI)*, 2020, pp. 558-562.

[46] M. Miri, *et al.*, "Enhanced motor imagery-based EEG classification using a discriminative graph Fourier subspace," *IEEE Int. Symp. Biomed. Imaging (ISBI)*, 2022, pp. 1-5.

[47] N. Perraudin, *et al*., "GSPBOX: A toolbox for signal processing on graphs," *arXiv preprint arXiv*, pp. 1408.5781, 2014.

[48] S. de Lange, *et al*., "The Laplacian spectrum of neural networks," *Front. Comput. Neurosci.*, vol. 7 , pp. 189, 2014.

[49] J.D. Medaglia, *et al*., "Functional alignment with anatomical networks is associated with cognitive flexibility," *Nat. Hum. Behav.*, vol. 2, no. 2, pp. 156-164, 2018.

[50] A.T. Jafadideh, and B. Mohammadzadeh Asl, "Rest-fMRI based comparison study between autism spectrum disorder and typically control using graph frequency bands," *Comput. Biol. Med.*, pp. 105643, 2022.

[51] H. Behjat, *et al*., "Signal-adapted tight frames on graphs," *IEEE Trans. Signal Process.*, vol. 64, no. 22, pp. 6017-6029, 2016.

SUPPLEMENTARY MATERIALS:

TABLE SI

NUMBER OF GRAPH EDGES FOR EACH SUBJECT AND ON AVERAGE ACROSS ALL SUBJECTS FOR THREE STUDIED GRAPHS. THE GL METHODS PRESERVE THE CONNECTIVITY OF THE GRAPHS BY USING A LOWER NUMBER OF EDGES COMPARED TO THE FULLY CONNECTED CORRELATION GRAPHS.

Graphs	*aa*	*al*	*av*	*aw*	*ay*	Mean ± std
log-penalized	1666	1756	2262	1322	1418	1684.8 ± 367.9
l_2-penalized	2468	2588	3108	2200	2232	2519.2 ± 366.9
correlation	13806	13806	13806	13806	13806	13806

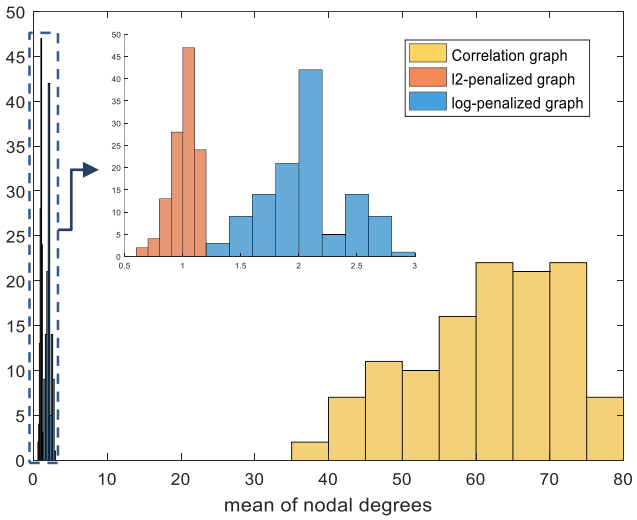

Fig. S1. Distribution of nodal degrees on average across five subjects. the log-penalized graphs are sparser graphs with larger edge weights compared to the l_2-penalized graphs and the fully connected correlation graphs.

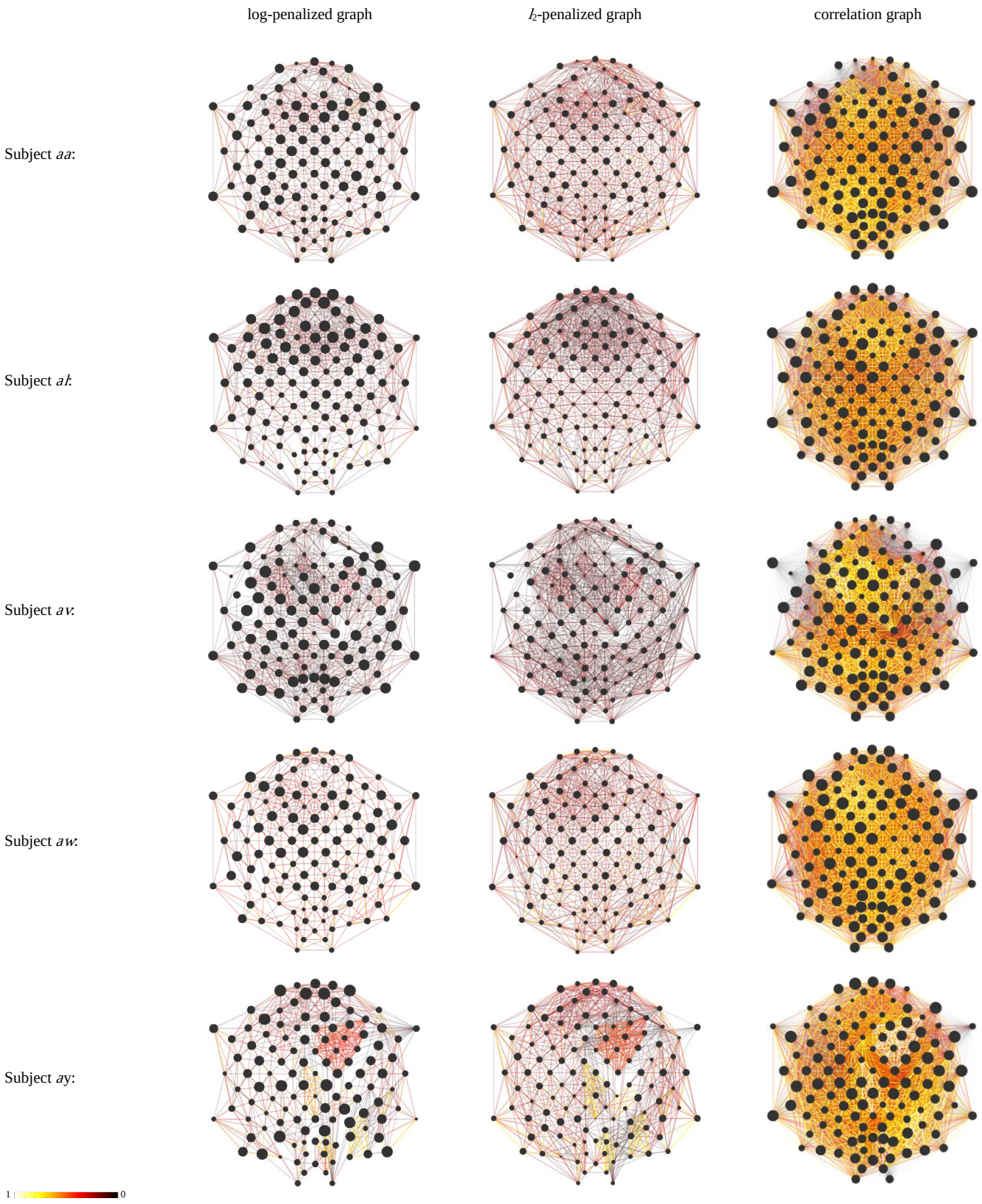

Fig. S2. The three studied brain graphs for each of the five subjects. Edge widths and colors reflect edge weights, and vertex sizes reflect nodal degrees. For the correlation graphs, only 50% of the top edges (with larger weights) are shown. In each type of graphs, differences are seen across the five subjects. the log-penalized graphs manifest a notable difference in their nodal degrees, and their structure in general, showing the added benefit of learning subject-specific graphs.

a) log-penalized graph:

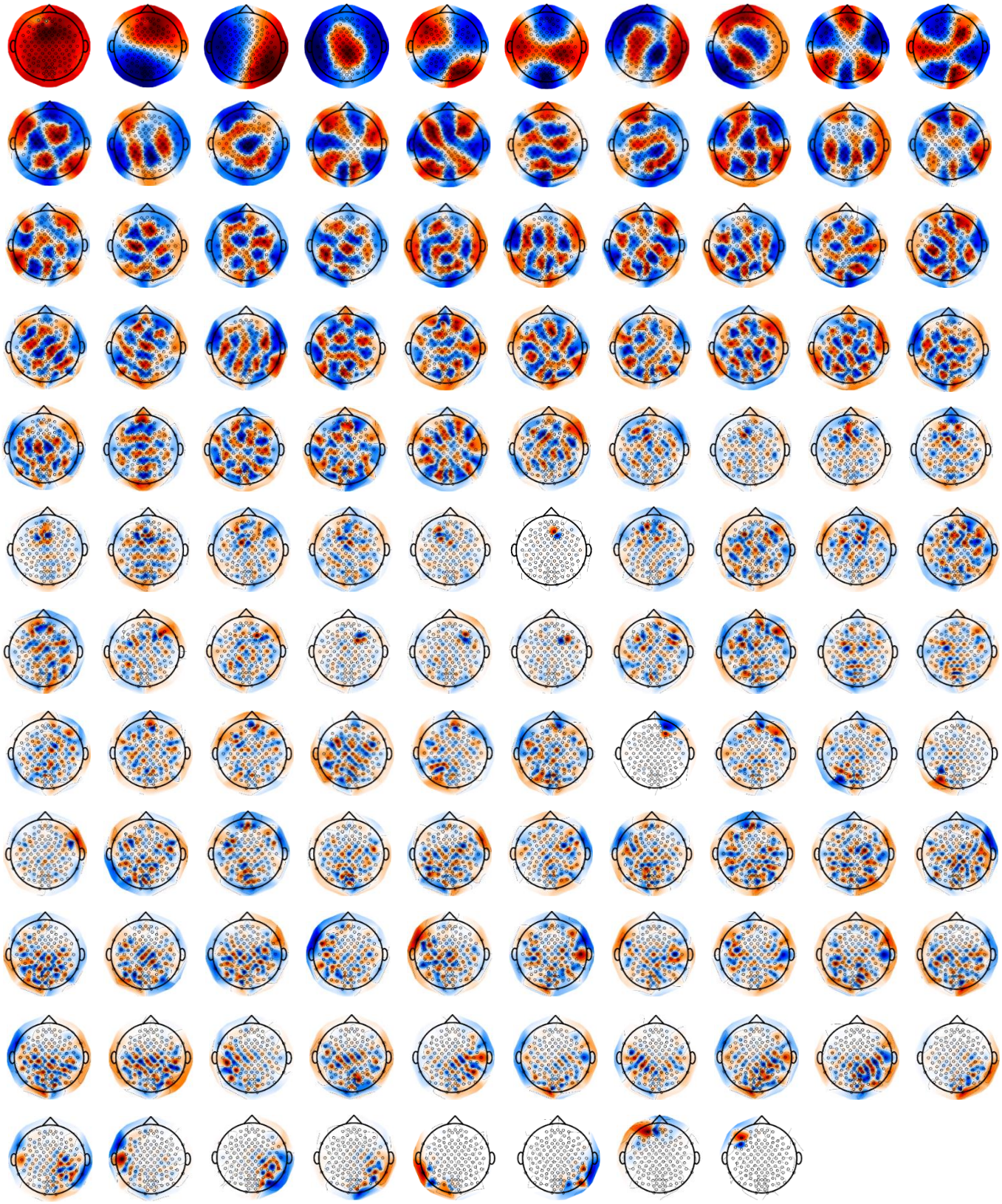

b) l_2-penalized graph:

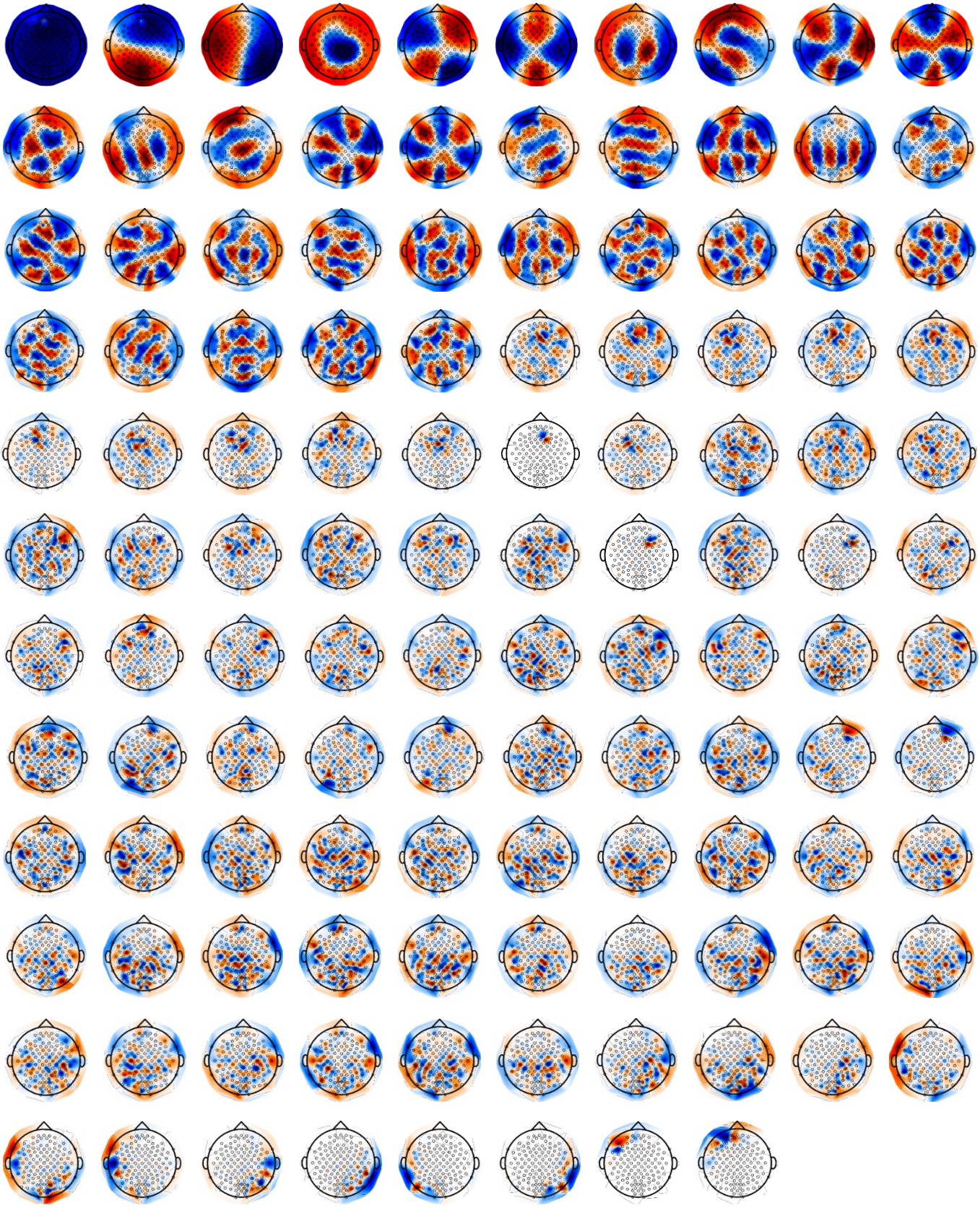

c) Correlation graph:

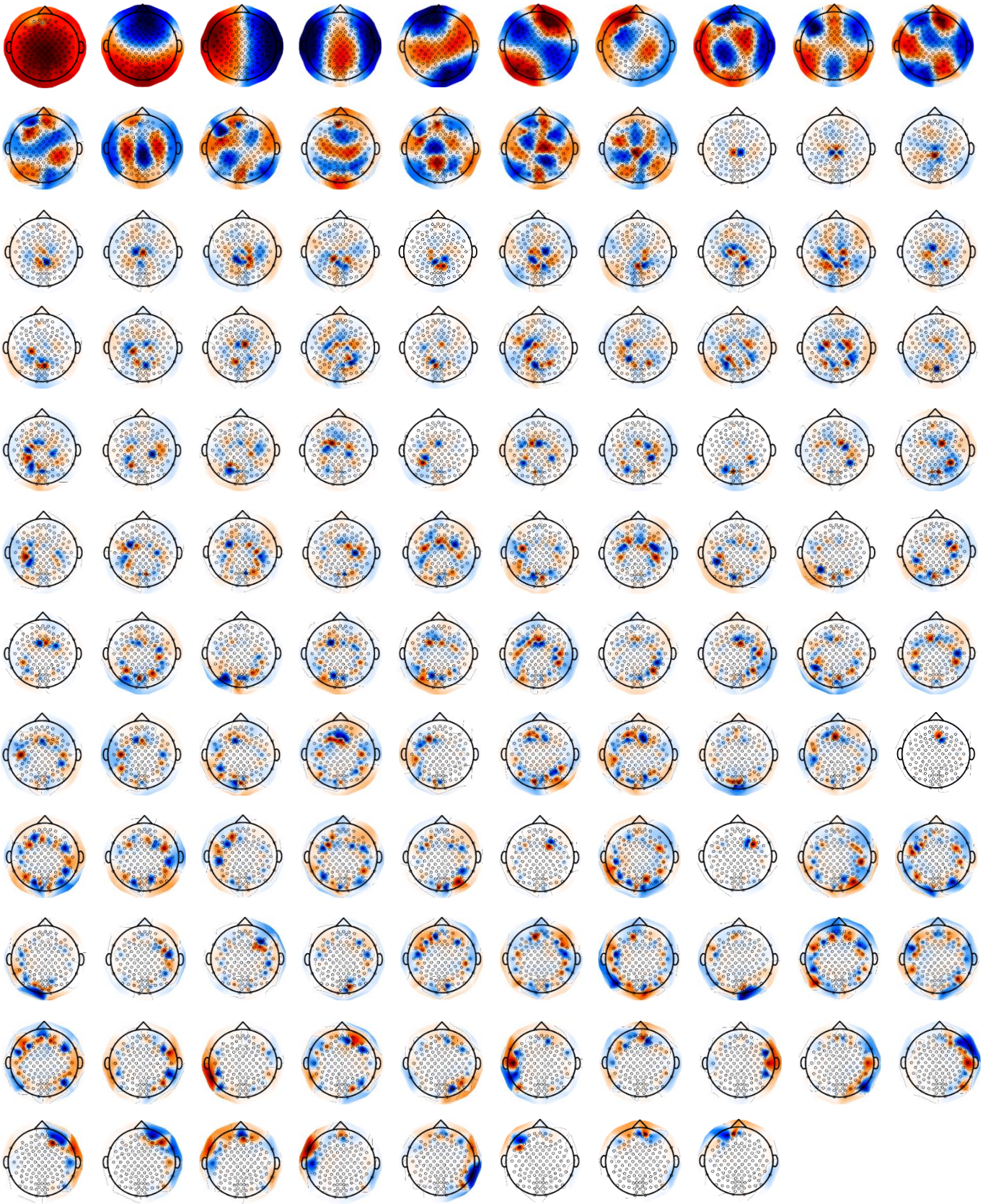

Fig. S3. The Laplacian eigenvectors of the (a) log-penalized, (b) l_2-penalized, and (c) correlation graphs for subject *aa*. There are remarkable differences in the spatial patterns encoded by the three different graphs. The eigenvectors of the learned graphs capture a wider range of spatial variability compared to the eigenvectors of the correlation graph which manifest rather repetitive patterns.

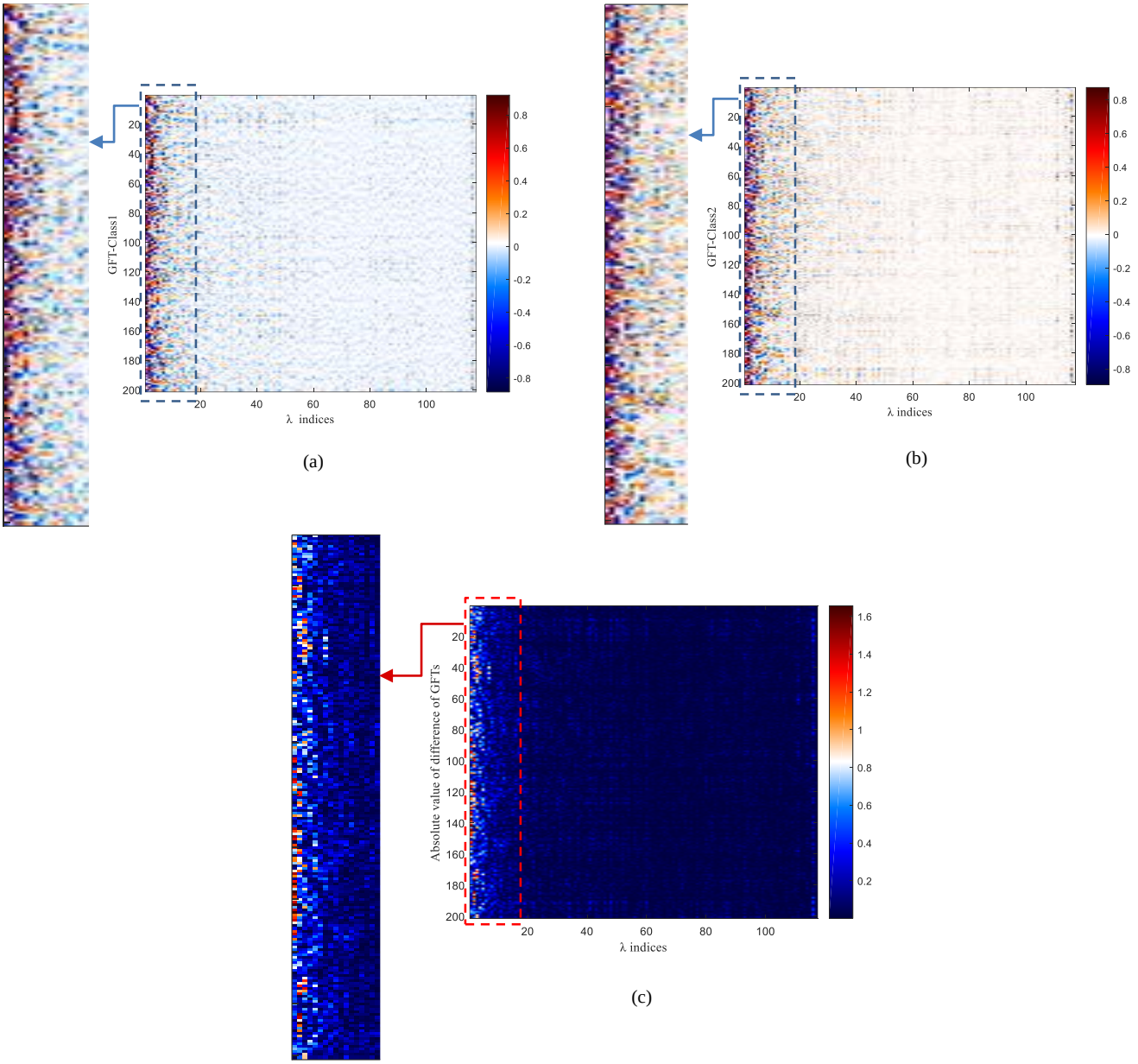

Fig. S4. (a, b) GFT coefficients of the log-penalized graph for a representative trial for each of the two MI classes of subject *aa,* and (c) the absolute value of the difference between the two. In the graph frequency domain, energy is localized in the lower end of the spectrum, where notable differences are seen between the two classes. The patterns are not constant across time, and this is what the FKT aims to capture in differentiating the two different MI tasks, which presumably manifest different temporal dynamics in their spatial manifestation in the EEG data.